Endoscopic sensing of alveolar pH

Endoscopic sensing of alveolar pH

D. Choudhury[1,2†], M. G. Tanner[1,2†], S. McAughtrie[2,3], F. Yu[4], B. Mills[2], T. R. Choudhary[2,5], S. Seth[6], T. H. Craven[2,7], J. M. Stone[4], I. K. Mati[3], C. J. Campbell[3], M. Bradley[2,3], C. K. I. Williams[6], K. Dhaliwal[2,7], T. A. Birks[4] and R. R. Thomson[*1,2]

[1]*Scottish Universities Physics Alliance (SUPA), Institute of Photonics and Quantum Sciences (IPaQS), Heriot-Watt University, Edinburgh, UK*
[2]*EPSRC IRC Hub, MRC Centre for Inflammation Research, Queen's Medical Research Institute (QMRI), University of Edinburgh, Edinburgh UK*
[3]*School of Chemistry, University of Edinburgh, Edinburgh UK*
[4]*Centre for Photonics and Photonic Materials, Department of Physics, University of Bath, Bath UK*
[5]*Institute of Biological Chemistry, Biophysics and Bioengineering, School of Engineering and Physical Sciences, Heriot-Watt University, Edinburgh, UK*
[6]*School of Informatics, University of Edinburgh, Edinburgh UK*
[7]*Pulmonary Molecular Imaging Group, MRC Centre for Inflammation Research, Queen's Medical Research Institute (QMRI), University of Edinburgh, Edinburgh UK*
*R.R.Thomson@hw.ac.uk
†*These authors contributed equally to this work*

Abstract: Previously unobtainable measurements of alveolar pH were obtained using an endoscope-deployable optrode. The pH sensing was achieved using functionalized gold nanoshell sensors and surface enhanced Raman spectroscopy (SERS). The optrode consisted of an asymmetric dual-core optical fiber designed for spatially separating the optical pump delivery and signal collection, in order to circumvent the unwanted Raman signal generated within the fiber. Using this approach, we demonstrate a ~100-fold increase in SERS signal-to-fiber background ratio, and demonstrate multiple site pH sensing with a measurement accuracy of ±0.07 pH units in the respiratory acini of an *ex vivo* ovine lung model. We also demonstrate that alveolar pH changes in response to ventilation.

OCIS Codes: (170.4580) (Primary) Optical diagnostics for medicine; (170.6510) Spectroscopy, tissue diagnostics.

References and Links

1. A. W. Ng, A. Bidani, and T. A. Heming, "Innate Host Defense of the Lung: Effects of Lung-lining Fluid pH," Lung **182**, 297–317 (2004).
2. C. R. Bodem, L. M. Lampton, D. P. Miller, E. F. Tarka, and E. D. Everett, "Endobronchial pH. Relevance of aminoglycoside activity in gram-negative bacillary pneumonia," American Review of Respiratory Disease **127**, 39–41 (1983).
3. A. A. Pezzulo, X. X. Tang, M. J. Hoegger, M. H. Abou Alaiwa, S. Ramachandran, T. O. Moninger, P. H. Karp, C. L. Wohlford-Lenane, H. P. Haagsman, M. van Eijk, B. Bánfi, A. R. Horswill, D. A. Stoltz, P. B. McCray, M. J. Welsh, and J. Zabner, "Reduced airway surface pH impairs bacterial killing in the porcine cystic fibrosis lung," Nature **487**, 109–113 (2012).
4. S. Jayaraman, Y. Song, and A. S. Verkman, "Airway surface liquid pH in well-differentiated airway epithelial cell cultures and mouse trachea," American Journal of Physiology - Cell Physiology **281**, C1504–C1511 (2001).
5. D. W. Nielson, J. Goerke, and J. A. Clements, "Alveolar subphase pH in the lungs of anesthetized rabbits," PNAS **78**, 7119–7123 (1981).
6. A. Dalhoff, S. Schubert, and U. Ullmann, "Effect of pH on the in Vitro Activity of and Propensity for Emergence of Resistance to Fluoroquinolones, Macrolides, and a Ketolide," Infection **33**, 36–43 (2005).
7. A. S. Trevani, G. Andonegui, M. Giordano, D. H. López, R. Gamberale, F. Minucci, and J. R. Geffner, "Extracellular Acidification Induces Human Neutrophil Activation," The Journal of Immunology **162**, 4849–4857 (1999).
8. W. F. Walkenhorst, J. W. Klein, P. Vo, and W. C. Wimley, "pH Dependence of Microbe Sterilization by Cationic Antimicrobial Peptides," Antimicrobial Agents and Chemotherapy **57**, 3312–3320 (2013).
9. A. Bidani and T. A. Heming, "Effects of bafilomycin A1 on functional capabilities of LPS-activated alveolar macrophages," Journal of Leukocyte Biology **57**, 275–281 (1995).

10. A. Bidani, B. S. Reisner, A. K. Haque, J. Wen, R. E. Helmer, D. M. Tuazon, and T. A. Heming, "Bactericidal Activity of Alveolar Macrophages is Suppressed by V-ATPase Inhibition," Lung **178**, 91–104 (2000).
11. S. W. Bishnoi, C. J. Rozell, C. S. Levin, M. K. Gheith, B. R. Johnson, D. H. Johnson, and N. J. Halas, "All-Optical Nanoscale pH Meter," Nano Lett. **6**, 1687–1692 (2006).
12. F. Wang, R. G. Widejko, Z. Yang, K. T. Nguyen, H. Chen, L. P. Fernando, K. A. Christensen, and J. N. Anker, "Surface-Enhanced Raman Scattering Detection of pH with Silica-Encapsulated 4-Mercaptobenzoic Acid-Functionalized Silver Nanoparticles," Anal. Chem. **84**, 8013–8019 (2012).
13. Y. Liu, H. Yuan, A. M. Fales, and T. Vo-Dinh, "pH-sensing nanostar probe using surface-enhanced Raman scattering (SERS): theoretical and experimental studies," J. Raman Spectrosc. **44**, 980–986 (2013).
14. P. L. Stiles, J. A. Dieringer, N. C. Shah, and R. P. Van Duyne, "Surface-Enhanced Raman Spectroscopy," Annual Review of Analytical Chemistry **1**, 601–626 (2008).
15. E. Garai, S. Sensarn, C. L. Zavaleta, N. O. Loewke, S. Rogalla, M. J. Mandella, S. A. Felt, S. Friedland, J. T. C. Liu, S. S. Gambhir, and C. H. Contag, "A Real-Time Clinical Endoscopic System for Intraluminal, Multiplexed Imaging of Surface-Enhanced Raman Scattering Nanoparticles," PLoS ONE **10**, e0123185 (2015).
16. Y. W. Wang, A. Khan, S. Y. Leigh, D. Wang, Y. Chen, D. Meza, and J. T. C. Liu, "Comprehensive spectral endoscopy of topically applied SERS nanoparticles in the rat esophagus," Biomed. Opt. Express **5**, 2883 (2014).
17. A. Ricciardi, A. Crescitelli, P. Vaiano, G. Quero, M. Consales, M. Pisco, E. Esposito, and A. Cusano, "Lab-on-fiber technology: a new vision for chemical and biological sensing," Analyst **140**, 8068–8079 (2015).
18. P. R. Stoddart and D. J. White, "Optical fibre SERS sensors," Anal. Bioanal. Chem. **394**, 1761–1774 (2009).
19. E. J. Smythe, M. D. Dickey, J. Bao, G. M. Whitesides, and F. Capasso, "Optical Antenna Arrays on a Fiber Facet for in SituSurface-Enhanced Raman Scattering Detection," Nano Lett. **9**, 1132–1138 (2009).
20. D. I. Ellis, D. P. Cowcher, L. Ashton, S. O'Hagan, and R. Goodacre, "Illuminating disease and enlightening biomedicine: Raman spectroscopy as a diagnostic tool," Analyst **138**, 3871–3884 (2013).
21. J. T. Motz, M. Hunter, L. H. Galindo, J. A. Gardecki, J. R. Kramer, R. R. Dasari, and M. S. Feld, "Optical Fiber Probe for Biomedical Raman Spectroscopy," Appl. Opt. **43**, 542–554 (2004).
22. J. T. Motz, S. J. Gandhi, O. R. Scepanovic, A. S. Haka, J. R. Kramer, R. R. Dasari, and M. S. Feld, "Real-time Raman system for in vivo disease diagnosis," J. Biomed. Opt. **10**, 031113 (2005).
23. Y. Komachi, H. Sato, K. Aizawa, and H. Tashiro, "Micro-optical fiber probe for use in an intravascular Raman endoscope," Appl. Opt. **44**, 4722–4732 (2005).
24. S. Dochow, I. Latka, M. Becker, R. Spittel, J. Kobelke, K. Schuster, A. Graf, S. Brückner, S. Unger, M. Rothhardt, B. Dietzek, C. Krafft, and J. Popp, "Multicore fiber with integrated fiber Bragg gratings for background-free Raman sensing," Optics Express **20**, 20156–20169 (2012).
25. B. B. Praveen, C. Steuwe, M. Mazilu, K. Dholakia, and S. Mahajan, "Wavelength modulated surface enhanced (resonance) Raman scattering for background-free detection," Analyst **138**, 2816–2820 (2013).
26. H. Yan, C. Gu, C. Yang, J. Liu, G. Jin, J. Zhang, L. Hou, and Y. Yao, "Hollow core photonic crystal fiber surface-enhanced Raman probe," Appl. Phys. Lett. **89**, 204101 (2006).
27. X. Yang, C. Shi, R. Newhouse, J. Z. Zhang, and C. Gu, "Hollow-Core Photonic Crystal Fibers for Surface-Enhanced Raman Scattering Probes," International Journal of Optics **2011**, 1–11 (2011).
28. D. Pristinski and H. Du, "Solid-core photonic crystal fiber as a Raman spectroscopy platform with a silica core as an internal reference," Optics Letters **31**, 3246 (2006).
29. G. F. S. Andrade, M. Fan, and A. G. Brolo, "Multilayer silver nanoparticles-modified optical fiber tip for high performance SERS remote sensing," Biosensors and Bioelectronics **25**, 2270–2275 (2010).
30. D. Choudhury, J. R. Macdonald, and A. K. Kar, "Ultrafast laser inscription: perspectives on future integrated applications," Laser & Photon. Rev. **8**, 827–846 (2014).
31. J. Koivisto, X. Chen, S. Donnini, T. Lahtinen, H. Häkkinen, G. Groenhof, and M. Pettersson, "Acid–Base Properties and Surface Charge Distribution of the Water-Soluble Au_{102}(pMBA)$_{44}$ Nanocluster," J. Phys. Chem. C **120**, 10041–10050 (2016).
32. A. Jaworska, L. E. Jamieson, K. Malek, C. J. Campbell, J. Choo, S. Chlopicki, and M. Baranska, "SERS-based monitoring of the intracellular pH in endothelial cells: the influence of the extracellular environment and tumour necrosis factor-α," Analyst **140**, 2321–2329 (2015).
33. J. S. Hartley, S. Juodkazis, and P. R. Stoddart, "Optical fibers for miniaturized surface-enhanced Raman-scattering probes," Appl. Opt. **52**, 8388 (2013).
34. G. Schulze, A. Jirasek, M. M. L. Yu, A. Lim, R. F. B. Turner, and M. W. Blades, "Investigation of Selected Baseline Removal Techniques as Candidates for Automated Implementation," Appl. Spectrosc. **59**, 545–574 (2005).
    P. H. C. Eilers and H. F. M. Boelens, *Baseline Correction with Asymmetric Least Squares Smoothing* (Leiden University Medical Centre, 2005).
35. C. E. Rasmussen and C. K. I. Williams, *Gaussian Processes for Machine Learning* (MIT press, 2006).
36. E. M. Scarpelli, "Physiology of the alveolar surface network," Comparative Biochemistry and Physiology Part A: Molecular & Integrative Physiology **135**, 39–104 (2003).
37. J. C. Knight, "Photonic crystal fibres," Nature **424**, 847–851 (2003).
38. A. Marcinkevičius, S. Juodkazis, M. Watanabe, M. Miwa, S. Matsuo, H. Misawa, and J. Nishii, "Femtosecond laser-assisted three-dimensional microfabrication in silica," Optics Letters **26**, 277–279 (2001).
39. S. Grant and R. S. Glass, "Sol-gel-based biosensor for use in stroke treatment," IEEE Transactions on Biomedical Engineering **46**, 1207–1211 (1999).

1. Introduction

The distal lung alveolar acinar regions are responsible for gas exchange. In health, the acini are devoid of infiltrating inflammatory cells and pathogens, while in inflammatory lung diseases such as pneumonia, the pathological hallmark involves dense infiltration by myeloid derived peripheral blood cells. These infiltrating cells have an arsenal of microbicidal targeted killing mechanisms including oxidative and proteolytic secretomes, which have the potential to drastically perturb physiological homeostasis in the alveoli and also induce host tissue damage. In pulmonary diseases characterized by inflammation and infection, homeostatic baselines of physiology may be significantly off-set, yet in trying to understand human disease, many biological processes are modeled *in vitro* with little knowledge about the physiological state of the distal lung due to the inability to concurrently access the alveolar sacs and perform real-time sensing. pH is a key parameter that is tightly regulated in cells and microenvironments. In the lung, a thin film of airway surface liquid lines the air-facing surface of the lungs. The conducting airways are lined with a mucus gel-aqueous sol complex of up to 100 microns in depth called air surface liquid (ASL) whilst the alveolar regions are lined with a complex of alveolar subphase fluid (AVSF) and pulmonary surfactant [1]. ASL pH is acidic compared to blood pH and *in vivo* in healthy humans ASL has been recorded as 6.6 using a bronchoscopically-deployed pH electrode [2]. In preclinical models, the ASL pH has been measured to be between 6.8 and 7.1 [3] and has also been shown to be responsive to changes to blood pH as well as to apical challenges of acid and alkali [1,4]. In contrast, current understanding of the AVSF is limited by the technological hurdles of measuring pH in the distal lung. Studies suggest that the AVSF pH is 6.9 in anesthetized rabbits [1,5].

Environmental pH may be a determinant of effective host innate defense against invading pathogens, with acidic pH having pleiotropic effects on encouraging bacterial growth, inactivating antibiotics and promoting resistance [2,6], reducing the clearance of neutrophils in inflammatory foci and promoting host damage through enhancing neutrophil activation and delaying apoptosis [3,7], reducing the microbicidal activity of endogenous cationic antimicrobial peptides [1,4,8] and impairing alveolar macrophage function [9,10]. Hence, the ability to quantify and monitor AVSF pH could provide a key biomarker of distal lung innate defense. Since such measurements have previously been impossible to achieve due to technological constraints, the aim of this work was to engineer and evaluate a 'first-in-class' alveolar pH sensor with high sensitivity and the ability to serially measure alveolar pH.

Due to the sequential branching and ever decreasing size of the respiratory tract, the terminal entry to alveoli is best achieved through a transbronchial approach with a small diameter optical fiber. Hence in this work, a pH sensing optrode was engineered to be compatible with a bronchoscope that could navigate to the 3rd order bronchi prior to extending the optrode into the respiratory acinar units. The prerequisites of the optrode included robust packaging to ensure the chemical sensors remain attached at the distal end, the ability for the optrode to measure pH in disparate bronchopulmonary segments and a high degree of sensitivity.

2. Sensing mechanism, instrument design and fabrication

We report the experimental implementation of a bronchoscope-deployable optical fiber based pH sensing probe (an optrode), and the validation of the optrode in a whole *ex vivo* ovine lung model (Fig. 1). The 1.2 mm wide optrode operates using 150 nm gold nanoshells deposited on the distal-end of the optrode, functionalized with para-mercaptobenzoic acid (p-MBA), a molecule that has been well characterized as being sensitive to pH changes in the physiological range [11-13]. The pH response of the p-MBA molecule can be interrogated by

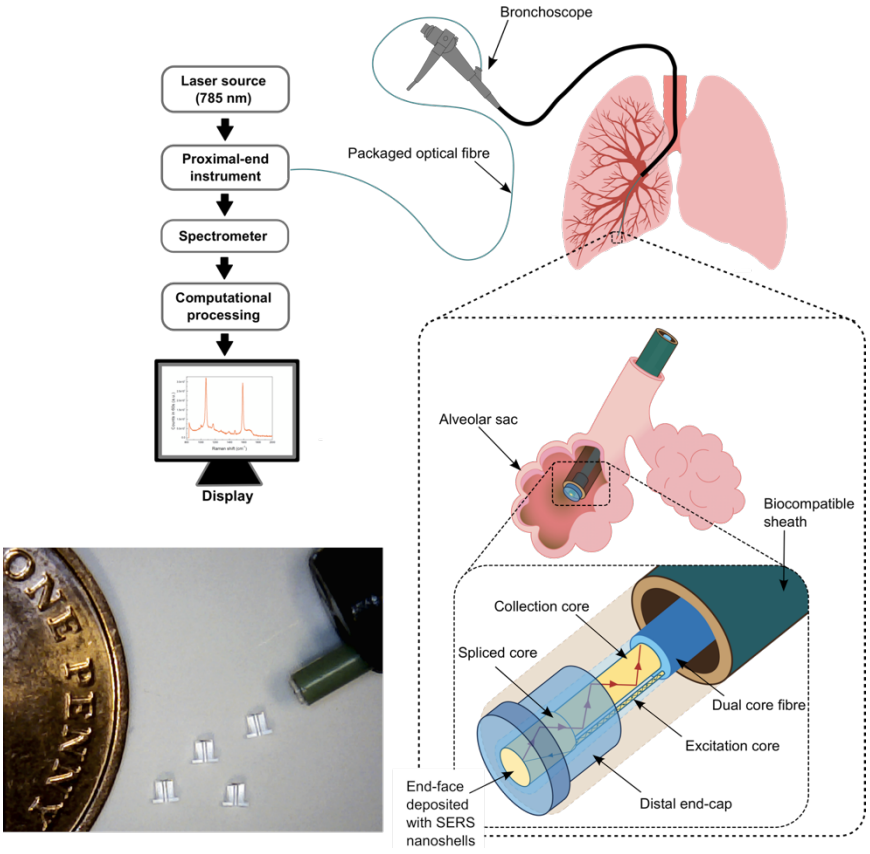

Fig. 1 Schematic illustration of the fiber-optic sensing system and the miniaturized optrode for measuring alveolar pH. The packaged miniaturized optrode consisted of a 3 m long custom fabricated asymmetric dual core optical fiber (outer diameter: 125 μm) and a bespoke distal end cap (outer diameter: 1.2 mm), assembled within a biocompatible tube (PEEK, outer diameter 1.5 mm). The fiber consists of a 2 μm diameter graded-index pump core (single mode at 785 nm) and a 28 μm diameter graded-index collection core that is multi-mode at the pump and signal wavelengths. The optrode was constructed by fusion splicing a short (~ 1 mm) section of a commercial multi-mode fiber (core diameter 50 μm, outer diameter 125 μm) onto the dual core fiber. The end-face of the optrode was deposited with Au nanoshells functionalized with p-MBA as the pH sensing reporter molecule. The fiber-optic optrode was navigated through the working channel of a standard bronchoscope into the alveolar space of an *ex vivo* ovine lung model. A proximal end optical instrument (see Fig. 2) was built to collect and direct the SERS spectra encoding the pH information to a spectrometer. Post-acquisition, the data was processed using machine-learning algorithms to predict the unknown pH in the distal lung. Inset photograph: The packaged optrode emerging from the accessory channel of a bronchoscope. 4 distal end-caps are also shown alongside a one-penny coin.

exciting it using a spectrally narrow optical pump, in order to generate a Raman spectrum of the molecule. The strength of the Raman signal is dramatically increased by spectrally tuning the pump signal to match the plasmonic resonance of the gold nanoshells (785 nm), a process known as surface enhanced Raman spectroscopy (SERS). There are multiple potential benefits of using SERS-based sensing as an analytical technique. For example, the spectral signatures from Raman-active analytes can be detected with exceptional sensitivity and specificity [14] due to the plasmonic enhancement of the otherwise weak Raman signal. Furthermore, SERS sensors offer the inherent possibility for multiplexed sensing. Whilst the endoscopic application of a SERS based fiber-optic sensor was recently demonstrated in *ex vivo* animal tissue, it was based on the local delivery of SERS nanoparticles [15], while the large lateral

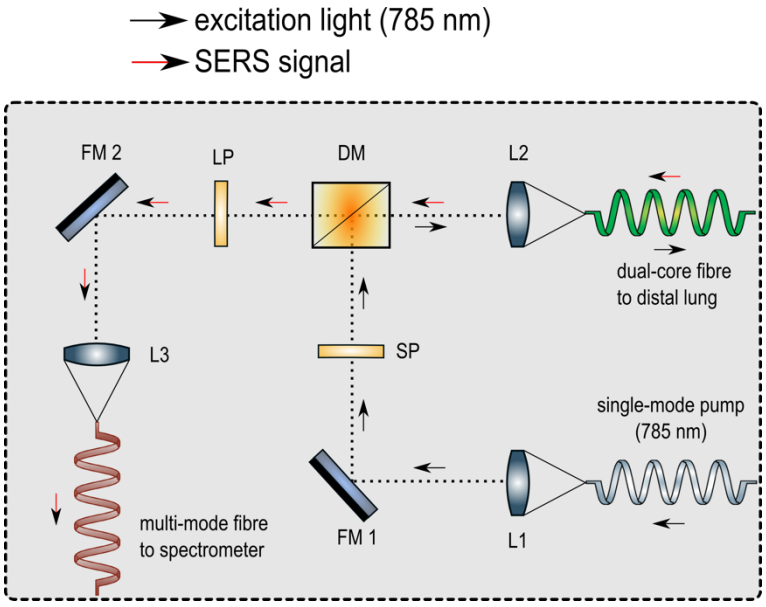

Fig. 2 A proximal-end optical instrument was used to input couple the excitation light into the SM core of the dual-core fiber and output couple the Raman-shifted signal light to the spectrometer. A continuous-wave 785 nm laser source (Thorlabs) with linewidth <0.1 nm was used as the pump source for this experiment. The 785 nm mode from a SM fiber (Thorlabs, 780-HP) was imaged at unit magnification using aspheric lenses (L1 & L2) onto the SM excitation core at the proximal end of the dual-core fiber. The SERS signal light from the MM core of the optrode was collected using lens L2 and, after passing through a long pass dichroic (DM), was imaged with unit magnification using the lens L3 and a fold mirror (FM 2) onto the step-index 50 µm core of a MM patch-cable which was attached to a spectrometer (Ocean Optics, QE Pro - 50 µm slit). In this background-suppressed mode, light in the SM core is explicitly excluded from being collected and routed to the spectrometer. Adjustment of fiber alignment allowed the instrument to be switched between background suppressed, and a more conventional non-suppressed mode, in which the same multi-mode core could be used for both excitation and collection. A short-pass filter (SP) was placed in the pump path before the dichroic to prevent the SERS signal being contaminated by long wavelength amplified spontaneous emission from the laser source. A long-pass filter (LP) was placed in the signal path to prevent 785 nm light from being coupled into the spectrometer. The spectral resolution was limited by the spectrometer to ~0.4 nm, narrower than the observed SERS spectral features (see Fig. 3c).

dimension of this instrument (5.3 mm) precludes its use in the distal lung (alveoli) and other anatomical sites where miniaturization is required for access and safety. An endoscopic imaging system (lateral dimension 2.5 mm) using 37 optical fibers was recently demonstrated to visualize topically applied SERS nanoparticles in the rat esophagus [16]. Although using more collection paths enables higher signal collection efficiency, there is clearly a trade-off between increased signal collection and engineering a sufficiently compact distal probe that can be accommodated within the alveolar microenvironment.

The possibility of combining the sensitivity of SERS sensors with the flexibility of optical fibers, has led to the emergence of lab-on-fiber technology [17]. For *in vivo* applications, an end-coupled optrode sensing scheme [18,19] is well-suited, as it enables the use of a single optical fiber to deliver (collect) the pump (signal) light to (from) the SERS sensors on the distal facet. However, the practical realization of this has proved difficult due to the intrinsic Raman signal generated by the fiber itself. In the low wavenumber region (≤ 2000 cm^{-1}) [20], SERS spectra acquired using bidirectional optrodes are accompanied by an intense broad continuum due to inelastic scattering from Raman-active material of the fiber core (typically doped silica) along which guided mode(s) of the monochromatic excitation pump light propagate(s). This background Raman spectrum can be overwhelming due to the long interaction length in the

fiber, and has imposed limitations on the optrode sensing scheme. Several probe designs to circumvent this problem have been investigated [21-28], but these solutions are relatively bulky (multi-fiber, large bore) and therefore not suitable for alveolar pH sensing [18,29]. With the future clinical impact of SERS-on-a fiber optrodes in mind, an additional key factor that must also be considered is manufacturability. The ideal technology would, for example, require only a single fiber, with only minimal additional packaging requirements.

To address the points outlined above, we have designed and fabricated an asymmetric dual core optical fiber, the cross section of which contains a 2 μm diameter single-mode core (SM at 785 nm) for pump delivery and excitation of the SERS sensors at the distal end, and a 28 μm multimode (MM) core for the collection of the SERS signals and transportation to diagnostics at the proximal end (see Fig. 2). To provide a platform for the deposition of the SERS sensors, a short length (~ 1.0 mm) of commercial MM fiber (50 μm diameter, step-index Ge-doped core, outer diameter of 125 μm) was spliced to the distal end of the dual-core fiber (see Fig. 1). The loss across this splice for 785 nm light was measured to be < 0.5 dB for 785 nm light contained in the 28 μm core, while the measured loss in the reverse direction was ~6 dB, consistent with that expected due to the geometric difference between the core dimensions in the current design. In the future, we expect that this loss can be significantly reduced through optimized design and fabrication of the dual-core fiber. The length of the MM fiber was only ~0.03 % the length of the dual-core fiber (3 m), and was deliberately kept short to minimize any Raman background originating from it. This short length was still observed to be sufficient to ensure high spatial overlap of the mode structure at the distal end-facet generated by the SM pump excitation and the region from which the MM core can collect SERS signal. This optrode design ensures that the large amount of silica background Raman signal generated in the excitation core by the pump was not collected and transmitted to our spectrometer by the collection core. The fiber was fabricated from pure silica with high index Ge-doped silica regions forming our two cores. Our excitation core was offset from the center of the fiber and the much-larger collection core was positioned in the center of the fiber (see Section A.1 for fabrication details). The effective diameter encircling the excitation and collection cores was 47 μm and the outer diameter of the fiber was 125 μm.

To provide structural robustness and functional preservation of the probe during repeated transbronchial passes which are required to access the distal lung, the spliced MM section was accommodated in a bespoke fused silica end-cap, which was fabricated using ultrafast laser inscription and selective chemical wet-etching [30] (Fig. 1 inset photograph, see Section A.2 for details). After an intermediate assembly step, a 20 μm^3 recess was machined into the facet of the 50 μm MM core using 800 nm, femtosecond laser pulses. This end-preparation was primarily performed to reduce nanoshell loss during transbronchial passes. A secondary advantage is that the femtosecond machining process also roughens the glass surface, reducing the specular Fresnel reflection of the forward scattered Raman-background. The entire length of the fiber, together with the silica end-cap, was sheathed inside a biocompatible polymer (PEEK tubing) with a total outer diameter of 1.5 mm, a diameter compatible with the working channel of most bronchoscopes. p-MBA functionalized Au nanoshells were deposited onto the end-prepared facet of the optrode, which was pre-treated with poly-L-lysine to augment adherence of the nanoshells to the machined silica surface. Finally, the end-facet of the miniature probe was encapsulated with a permeable sol-gel layer to further inhibit contact-induced nanoshell loss.

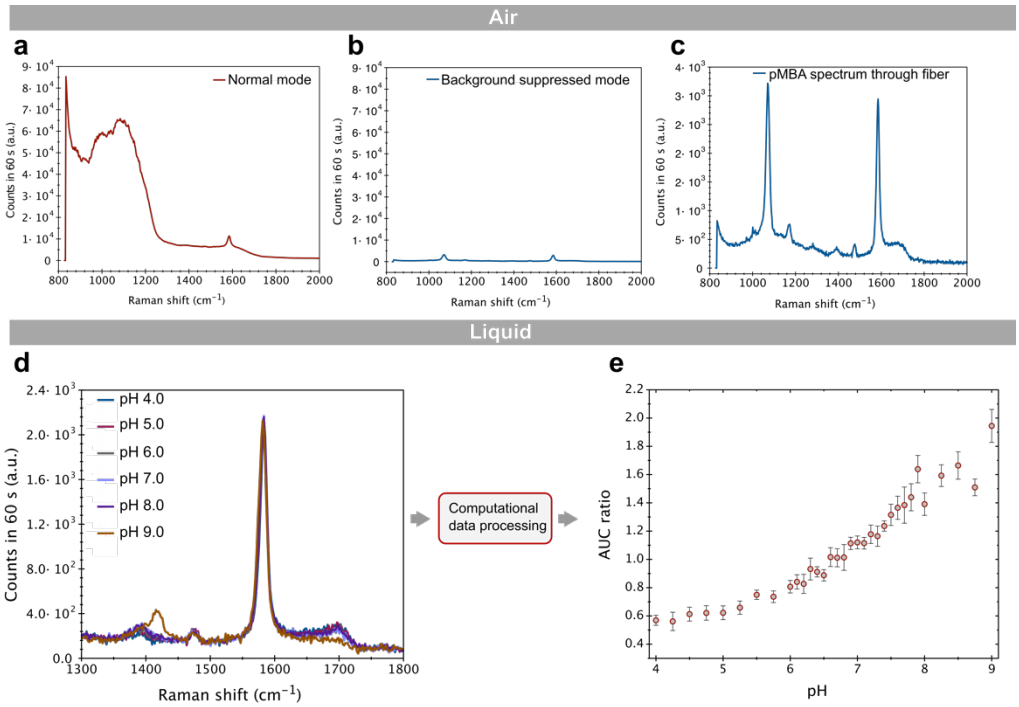

Fig. 3 Background suppressed p-MBA SERS spectrum and its characteristics with respect to change in pH, observed using the packaged fiber-optic optrode. (a) p-MBA SERS spectrum acquired between 800 cm^{-1} and 2000 cm^{-1} when the MM core was used for both excitation and collection (normal mode). (b) p-MBA SERS spectrum acquired between 800 cm^{-1} and 2000 cm^{-1} when the SM and MM cores were used for excitation and collection respectively (background suppressed mode). Suppression of the fiber Raman background by ~ 100-fold was achieved in comparison to the spectrum shown in (a). (c) Characteristic p-MBA SERS spectrum acquired using the fiber-optic optrode. (d) p-MBA SERS spectrum from 1300 cm^{-1} to 1800 cm^{-1} showing pH sensitive response in the vicinity of 1380 cm^{-1} and 1700 cm^{-1}. (e) Variation of the area under the curve (AUC) ratio with respect to pH in the range 4.0 – 9.0 obtained after computational data processing (see Section 3.1.1). The error bars represent the standard error of the mean over five technical replicate measurements, acquired over measurement intervals up to 9 hours. The extended time intervals between replicate measurements increase the extent of error bars. The intrinsic accuracy of the SERS measurements is analyzed separately (see Section 3.1.3).

3. Results

3.1 On-bench instrument calibration

For all experiments, a pump wavelength of 785 nm was used, with a power of ~0.4 mW exiting the probe after absorption by the SERS nanoshells. Preliminary experiments indicated that this power would avoid degradation (due to heating) of the SERS signal. Comparative spectra obtained using the probe under normal and "background-suppressed" modes of operation (see Fig.2, Fig. 3a and Fig.3b) indicated a ~100-fold increase in SERS signal-to-fiber background ratio, whilst the SERS spectrum of the p-MBA molecule (Fig 3c) was almost completely identical to that recorded on gold-coated slides [13]. The variation of the p-MBA SERS spectrum obtained using the packaged miniaturized optrode was calibrated using buffers with pH values ranging from 4.0 to 9.0 (see Figures 3d and 3e). Under alkaline conditions (pH 9.0 and above), the p-MBA molecule is known to be mainly de-protonated [31], which results in a relatively stronger response to pH change as can be clearly seen for the peak at ~1420 cm^{-1} in Fig. 3d.

The raw spectra were analyzed in two ways (i) with simple subtraction of the spectral shape of a known fiber background, the magnitude of which was normalized to a reference Raman-shift

position (1070 cm^{-1}) that was known to be invariant with pH or (ii) computationally processed using machine learning algorithms devised to adaptively learn the pH driven

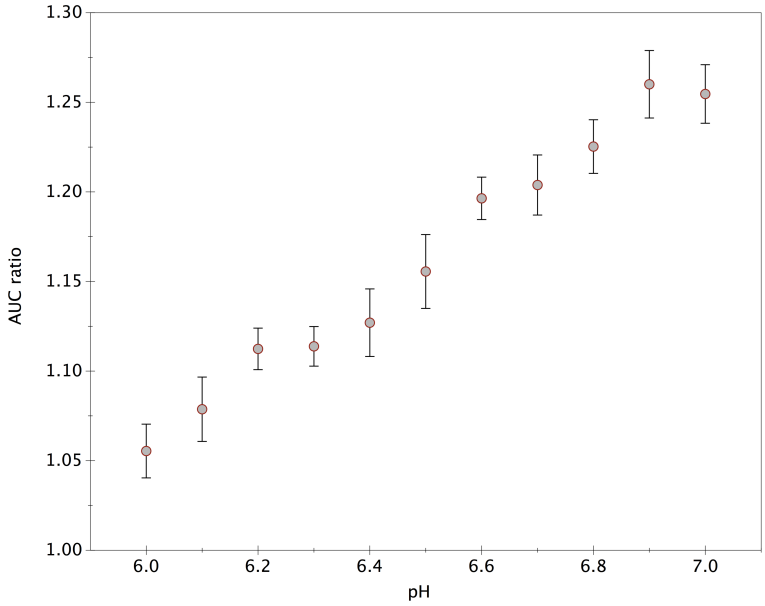

Fig. 4 Variation of area under the curve (AUC) ratio as a function of pH within the pH 6.0 – 7.0 range. The error bars represent the standard error of the mean over five technical replicate measurements, acquired over measurement intervals up to 4 hours.

changes, and remove the contribution of the spectra due to any residual fiber-background (see Section 3.1.2). The post-processed spectra were subsequently evaluated for ratiometric changes in the area under the curve (AUC), within a ±25 cm^{-1} window of the peaks at 1380 cm^{-1} and 1700 cm^{-1}, the spectral features known to be most sensitive to pH [32] (Fig. 3d) and demonstrated a clear and consistent variation within the physiologically relevant pH range (Fig. 3e). In a separate experiment, the intrinsic measurement accuracy of the probe at pH 6.4 and pH 7.4 was evaluated to be ± 0.07 pH units (see Section 3.1.3). The results obtained from a separate experiment within the pH 6.0 – pH 7.0 range, using 55 measurements and the same methodology as above is presented in Fig. 4.

3.1.1 Computational data processing

A typical background-suppressed SERS spectrum acquired using the fiber-optic probe is primarily composed of two components, the 'signal' component $s(x:pH)$ that originates due to the pH sensitive Raman response of the reporter molecules and a residual 'background' component $b(x)$ generated by the Raman active material of the fiber. Here, x denotes Raman shift in cm^{-1}. Throughout the following, we denote signal and background spectra as vectors of Raman intensities at predetermined Raman shifts. The scale of s depends on the density of the deposited reporter molecules and the scale of b is influenced by the length, material, mode structure and numerical aperture of the fiber core [33], while the scales of both s and b depend on the data acquisition time. Therefore, the components s and b exhibit scale indeterminacy, i.e. their accurate determination is limited by an unknown scaling factor. The respective contributions of b and s in the final spectrum $(\tilde{s})$ may vary between replicate measurements, especially if such measurements are spaced over extended time intervals, due to change in

single-mode input coupling or contact induced loss of reporter molecules. The final spectrum can therefore be expressed as follows:

$$\tilde{s}(pH,r) = c_s^r s(pH) + c_b^r$$

where $\tilde{s}$, b , s represent the final spectrum, the background and signal contributions respectively, c_b , c_s , are the strengths of the respective contributing spectra, and r denotes replicate.

Note: The exact shape of the p-MBA SERS spectrum is not known. This is counterintuitive, as the spectra (s) can be acquired from a functionalized slide instead of a fiber, which should in principle, reveal the spectral shape $(\tilde{s} = s)$ without the fiber background $(b = 0)$. However, we observed that the p-MBA spectra from functionalized slides acquired at different pH environments exhibit a non-vanishing lower envelope, which is similar but not identical between spectra. This finite offset may be attributed to being an inherent feature of the molecules' Raman signature, although some variable contribution due to instrument bias cannot be disregarded. Thus, any algorithmic estimation of signal characteristics (s) within the final spectrum $(\tilde{s})$ should optimally ascertain the degree to which the offset should be included in s or indeed merged with b .

The change in pH is estimated by observing the change in specific parts of the spectrum. Typically, we observed the two most pH sensitive spectral windows to be in the vicinity of 1380 cm^{-1} and 1700 cm^{-1} for the p-MBA reporter. Following Jaworska *et al*. [32], we compute the area under the Raman spectrum around these frequencies with a window size of 50 cm^{-1} to characterize a pH value.

3.1.2 Background shape estimation

Estimating the contribution of background in a SERS spectrum $(\tilde{s})$ is a well-studied problem in the literature [34], where established methods are based on the assumption that the background (b) is smooth, and that the SERS signal (s) is composed of peaks at characteristic frequencies, depending on the reporter molecule. These methods tend to work well when the aforementioned assumptions are satisfied and in particular, when one is interested in the well-defined 'narrow' peaks. However, in our observations, the spectral regions of interest in the vicinity of 1380 cm^{-1} and 1700 cm^{-1} are composed of 'broad' peaks, which cannot be discriminated well from a smoothly varying background (b) . Depending on the parameters of the background estimation method, these peaks of interest risk being incorporated in the background. Additionally, since such broad peaks are relatively less prominent, even slight variations in the estimated background (b) can lead to the poor estimation of signal characteristics. Thus, we observe that estimating the background (b) separately for each spectrum, usually leads to large variation in signal characteristics between replicate measurements. Therefore, to avoid this issue we jointly estimate the background (b) from multiple SERS spectra.

We applied adaptive iterative reweighted penalized least squares (airPLS) [35] in estimating the background (b) from the SERS signal $(\tilde{s})$ by minimising the following cost function:

$$(\tilde{s} - b)^T W(\tilde{s} - b) + \lambda \| \Delta^2 b \|^2$$

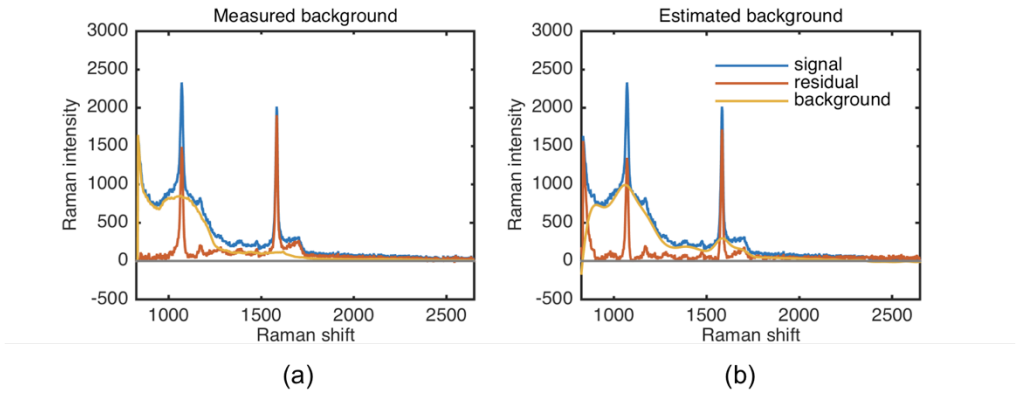

Fig. 5 Typical shape of p-MBA SERS, background and residual spectra acquired using the fiber optic optrode. The residual spectra were obtained using (a) a measured background spectrum and (b) background estimated using adaptive iterative reweighed penalized least squares, (airPLS). The measured background is subtracted by estimating its strength using airPLS by keeping the background (b) fixed and learning the coefficient (c_b^i). We observe that although the measured background exhibits a lower envelope of a typical p-MBA SERS spectrum (obtained through the fiber) at Raman shifts lower than 1200 cm^{-1}, it is not so at shifts higher than 1200 cm^{-1}.

where W is a diagonal matrix with entries $W_{ii} = p$ if $\tilde{s}i > b_i$ and $1-p$ otherwise, $\Delta^h b$ denotes a vector of h order differences between consecutive entries of b. Here the first term penalizes negative errors more than positive errors (by choosing $0 < p << 1$) thus estimating a lower envelope of the signal whereas the second term imposes a regularity constraint of the estimated background.

We modify this approach slightly to share background among several spectra as follows:

$$\sum_i (\tilde{s}^i - c_b^i b)^T W^i (\tilde{s}^i - c_b^i b) + \lambda \| \Delta^2 b \|^2$$

where $c_b^i b$ are strength of background b in spectra $\tilde{s}^i$. Notice that s_i denotes the i-th entry of vector s, and s^i denotes the i-th vector. After estimating the background, we ascertain the signal spectrum s^i as $s^i = \tilde{s}^i - c_b^i b$ and compute the subsequently relevant signal characteristics. Notice that in the case of a known background, b can be fixed, therefore only c_b^i's need to be learned. Fig. 5 illustrates the shape of a typical residual spectrum obtained by subtracting a measured background from the SERS spectrum and its comparison to the residual obtained when the background was estimated using airPLS.

3.1.3 Intrinsic measurement accuracy of the fiber-optic optrode

The *in vitro* measurements were performed over extended periods (pH 4.0 – 9.0: 9 hours and pH 6.0 – 7.0: 4 hours) where, due to the randomized nature of the measurements, the replicate spectra acquired for each pH were spaced apart by long time intervals. In order to determine the measurement accuracy of the fiber-optic optrode, we performed consecutive measurements at two pH values, 6.4 and 7.4 respectively, with each spectrum acquired over 60 seconds. The AUC ratio was observed to drift with time after 2 hours, thus samples of 50 spectra (acquired in less than 1 hour) were considered for assessing the measurement accuracy.

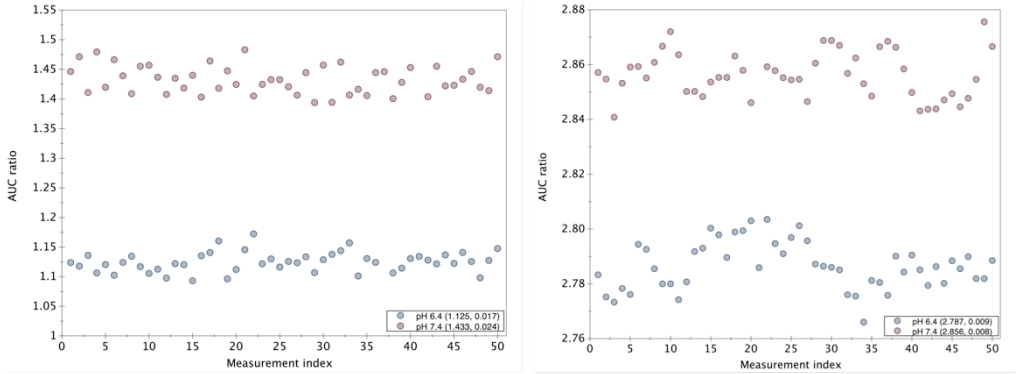

(a) (b)

Fig. 6 The area under the curve (AUC) ratio obtained at pH 6.4 and 7.4 plotted against time over 50 consecutive replicate measurements (a) with background suppression (b) without background suppression. The numbers in the insets represent the mean and standard deviation of the data for each pH respectively.

The AUC ratios were obtained for pH 6.4 and 7.4 using spectra acquired with (Fig. 6(a)) and without (Fig. 6(b)) background suppression. Computational data processing yielded the intrinsic measurement accuracy of the fiber-optic optrode to be 0.07 pH units compared to 0.12 pH units in the case where no background suppression was applied. In Fig. 3e it is clear that the results from replicate acquisitions have shifted during the course of the extended (9 hours) measurement. We therefore infer that the variance in the AUC ratio observed in the *in vitro* measurements shown in Fig. 3e and Fig. 4 are a consequence of the measurements being staggered over prolonged intervals. In this respect, factors such as ambient temperature induced shift in optical alignment to the SM fiber core and the sensitivity of the pH buffer to thermal currents caused by the laser irradiation, cannot be disregarded. However, these factors do not limit the intrinsic measurement accuracy of the technology being presented in this work.

3.2 Predicting unknown alveolar pH

The packaged miniaturized probe was recalibrated between pH 4.0 – 9.0 using pH buffers on the day of the ovine lung model experiments, data from which were subsequently used to analyze the spectra obtained from alveolar acinar units. To predict the unknown pH values in the ovine lung model experiments, the relationship between the AUC ratio and pH was modeled using Gaussian process regression [36] from an appropriate calibration dataset. We used the Matlab implementation available at the following link:

(http://www.gaussianprocess.org/gpml/code/matlab/doc/).

3.2.1 Evaluation and validation using an *ex vivo* ovine lung model

An *ex vivo* ventilated ovine lung model (Fig 7a) was used to demonstrate the feasibility of performing serial alveolar pH measurements in disparate bronchopulmonary segments of a human-size lung. Specifically, six distal subsegments (Fig. 7b) in the lung were first instilled with 10 mL of buffer solutions with pH values ranging from 2.0 to 12.0. The perfusion and ventilation circuits used for the model are illustrated in Fig. 7c. For the first experiment, the lung was not perfused in order to prevent the instilled solutions from accessing perfused vasculature and affecting other subsegments. After a 30-minute interval to permit self-

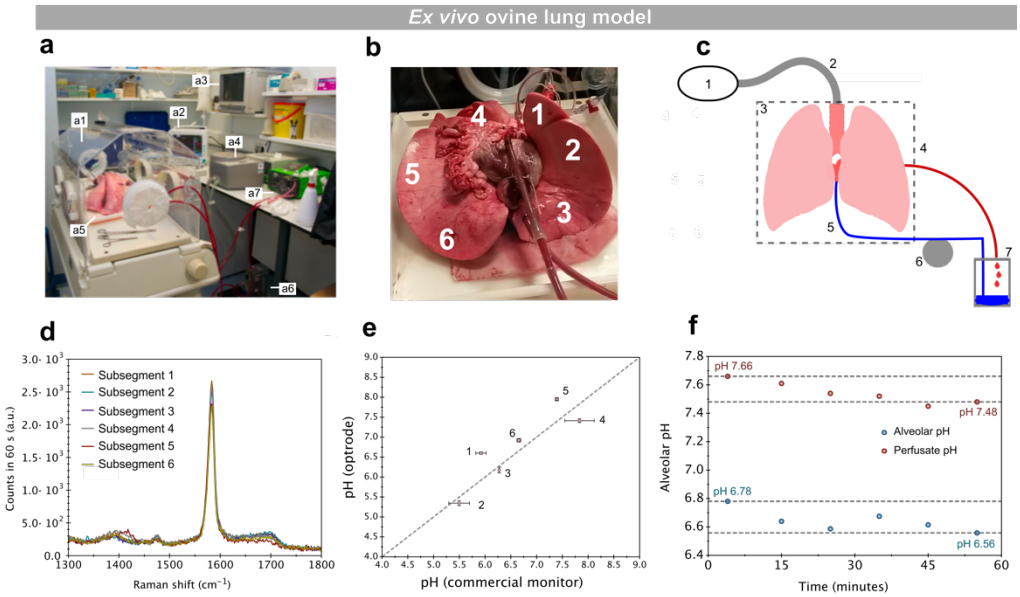

Fig.7 Alveolar space pH measured using the fiber-optic optrode in an *ex vivo* ovine lung model. (a) Photograph of the *ex vivo* ovine lung perfusion and ventilation set-up used for the experiment. **a1**: Incubator **a2**: Physiology monitor **a3**: Bronchoscopy screen **a4**: Ventilator and closed breathing circuit **a5**: Ventilated ovine lung **a6**: Water bath and perfusate circuit **a7**: Roller pump. (b) Photograph of the *ex vivo* ovine lung with numbers representing the six subsegments interrogated using the fiber-optic probe (c) Illustration showing the perfusion and ventilation circuits used in the experiment. 1: Ventilator, 2: Breathing circuit, 3: Incubator and humidifier, 4: Left atrial cannula, 5: Pulmonary artery cannula, 6: Roller pump, 7: Reservoir (d) p-MBA spectrum between 1300 cm^{-1} and 1800 cm^{-1}, obtained from the sequential interrogation of the six distal subsegments shown in (b). (e) The alveolar pH measured using the fiber-optic optrode for the six subsegments (y-axis). The x-axis represents the pH measured using the commercial pH monitor at the incised locations for each subsegment. The numbers indicate the order in which the instilled subsegments were interrogated using the fiber-optic optrode. (f) Alveolar pH variation as a function of time in an *ex vivo* ovine lung model with ceased ventilation (t = 0) measured using the fiber-optic optrode. The variation of perfusate pH with time measured using a commercial pH probe is also shown.

buffering, the subsegments were sequentially interrogated using the probe and spectra recorded with an integration time of 60 s using 0.4 mW of 785 nm coherent excitation light (Fig. 7d). To obtain these measurements, the working channel of a standard flexible bronchoscope was used to navigate the packaged fiber-optic probe through the bronchial tree
prior to a transbronchial pass into the alveolar space of each subsegment. Alveolar sensing was ensured through proximally wedging the bronchoscope in 3rd order bronchi and extending the optrode sheath a defined distance to reach the subpleural alveolar regions. For each subsegment, the location of the probe at the distal end was marked on the exterior of the lung and three spectra were obtained at each location. At the end of the experiment, three incisions were made within the vicinity (~ 5 mm) of each marked location and a commercial large-bore tissue pH monitor (Mettler Toledo) was used to measure the pH in the respective subsegments. The decision to objectively validate the optical measurements using multiple closely-spaced incisions was primarily based on the large difference in bore diameter between the two probes and the consequent impracticality of precisely determining (within millimeters) the exact location in the alveoli where the fiber-optic interrogation was performed. For the six subsegments interrogated using the fiber-optic probe, the alveolar pH evaluated from the spectral AUC ratio was found to be in good agreement with the pH measured using the commercial probe (Fig. 7e). Each subsegment showed the expected deviation in pH from that of the pre-instilled fluid due to self-buffering, while in 3 subsegments (1, 2 and 4), the pH

measured using the commercial probe revealed notable variations (>0.8 pH units) across a short spatial measurement range (<1 cm). These variations resulted in an apparent lowering in correlation between the validation and optrode measurements.

3.2.2 Monitoring the effect of ventilatory arrest on alveolar pH using a perfused and ventilated *ex vivo* ovine lung model

A second experiment was conducted using an *ex vivo* lung perfusion (EVLP) and ventilated model in which ventilation was stopped, in order to demonstrate the sensitivity of the optrode to temporal variations in the distal lung pH and also to observe if blood pH and alveolar pH are correlated. In this experiment, a single subsegment in the lung was selected and the optrode was positioned in the subpleural alveolar region through the working channel of the bronchoscope. Over the duration of 60 minutes, samples of perfused blood were extracted at 10-minute intervals and the pH measured with a commercial pH probe while alveolar SERS spectra were concurrently acquired using the optrode. The temporal variations in alveolar pH were consistent with that of perfused blood, with both measurements showing a correlated reduction in pH when ventilation was ceased (Fig. 7f).

4. Discussion

Understanding alveolar physiology in humans is an important scientific endeavor. Alveolar pH is a key determinant of host innate defense against microbial challenge. The increasing and inexorable rise of antimicrobial resistance necessitates efforts to better define and develop strategies to augment host defense and hence the temporal measurement and potential manipulation of pH in the lung may represent an alternative strategy to augment host defense. Current pulmonary sampling approaches such as bronchoalveolar lavage, transbronchial lung biopsy or transbronchial needle aspiration are not appropriate for bedside *in situ* physiologic monitoring and aspirate samples are ordinarily examined using *in vitro* cytologic and histochemical methods. Moreover, the pH of post-aspirated fluid or biopsies are not representative of the pH of the endogenous and epithelial lining fluids within the alveolar environment due to the intrusive nature of the aspiration process and uncertainties such as aspirate sampling, volume, dilution and temperature. Whilst there have been some attempts at measuring ASL pH in both preclinical and clinical environments[2,3], there have been no descriptions of serial alveolar pH measurements.

Current knowledge of alveolar physiology is based upon *in vitro* models and also ultrastructural imaging of fixed and processed samples [37]. This has led to conjecture about the consequences of inflammation and disease on pH in the AVSF [1]. The work presented here focused on developing a robust engineering platform to provide an approach for measuring alveolar pH. We chose to use SERS chemical sensors as they provide exceptional sensitivity alongside with future multiplexing capability. A big challenge with optical fiber-based SERS sensing is the sufficient removal of background Raman from the fiber and to overcome this, we deployed a simple and compact optrode design to enable a ~100-fold increase in SERS signal-to-fiber background ratio, and delivered a pH accuracy of ± 0.07 pH units.

We tested the optrode in a large lung model to simulate technical challenges likely to be encountered in human lung sensing. The major findings of this work include the demonstration of high sensitivity and accuracy of the optrode in measuring alveolar AVSF pH. Disparate measurements in distinct bronchopulmonary segments after acid and alkali challenge alongside the temporal response of acidification of the AVSF in response to hypoventilation provide strong evidence of potential performance capability.

Further testing is now required *in vivo* in primary models of disease and human lungs to further test performance and to provide for the first time *in situ* human alveolar pH sensing. For clinical translation, the nature of the technological solution is an invasive medical device, which now requires to undergo biocompatibility, sterilization validation and also safety assessment prior to

entering clinic followed by iterative clinical evaluation in phased studies. The small quantity of SERS particles that are immobilized at the distal tip are unlikely to cause pulmonary toxicology but formal toxicology is required. As no 'gold-standard' currently exists for human alveolar pH, an inherent challenge will be ongoing calibration to ensure that the system performance is deemed to be acceptable in clinical trials.

5. Conclusion

The optrode demonstrated here is a generic platform that can be multiplexed with other SERS reporters to enable the concurrent *in vivo* and *in situ* monitoring of additional physiologically relevant parameters in the alveolar space such as oxygen tension and glucose levels. The observed factor of ~100-fold improvement in signal to background, implies that the measurement is no longer limited by the Raman contribution from the fiber. We emphasize that future work will aim to increase the efficiency of the SERS signal collection at the distal-end, for example through further optimization of the number of collection cores, their shape and geometry, and by making more use of the space currently unused at the distal-end. This technological advance will be even more important for SERS molecular reporters with signal features at lower Raman shift, where fiber background is orders of magnitude larger. It is envisaged that with further development and ongoing improvements in SERS sensitivity and optical performance, this technology platform has the potential to complement endoscopic procedures and generate novel and unique signatures of distal lung physiology, in order to improve our understanding of pulmonary biology.

Funding

The authors gratefully acknowledge the UK Engineering and Physical Sciences Research Council (EP/K03197X/1) for funding this work.

Author contributions

DC and MGT performed the instrumentation development and optrode characterization, *ex vivo* experiments and data analysis. DC developed the end-cap, the optrode and prepared the manuscript. MGT coordinated experiments at the QMRI. SM and MGT performed preliminary SERS on fiber *ex vivo* pH tissue measurements. FY designed, fabricated and tested the dual core fiber. JMS designed the dual core fiber. SM, IKM and CJC optimized the p-MBA functionalized nanoshells, fiber deposition protocols and characterization. SS and CKIW developed computational algorithms for data analysis. BM, THC and TRC designed and performed *ex vivo* lung experiments. TAB and RRT conceived the asymmetric dual core fiber. MB and KD provided strategic oversight. KD designed the *ex vivo* experiments and contributed to manuscript preparation and generated biological hypothesis. RRT led the optrode development and testing and the writing of the manuscript. All authors discussed the results and commented on the manuscript.

Competing financial interests

The authors declare that they have no competing financial interests. UK Patent application (number 1604331.7) pertaining to the background suppression method has been filed.

Code availability

The code will be made available via Edinburgh DataShare.

Data availability

The experimental data will be made available via Edinburgh DataShare.

Appendix

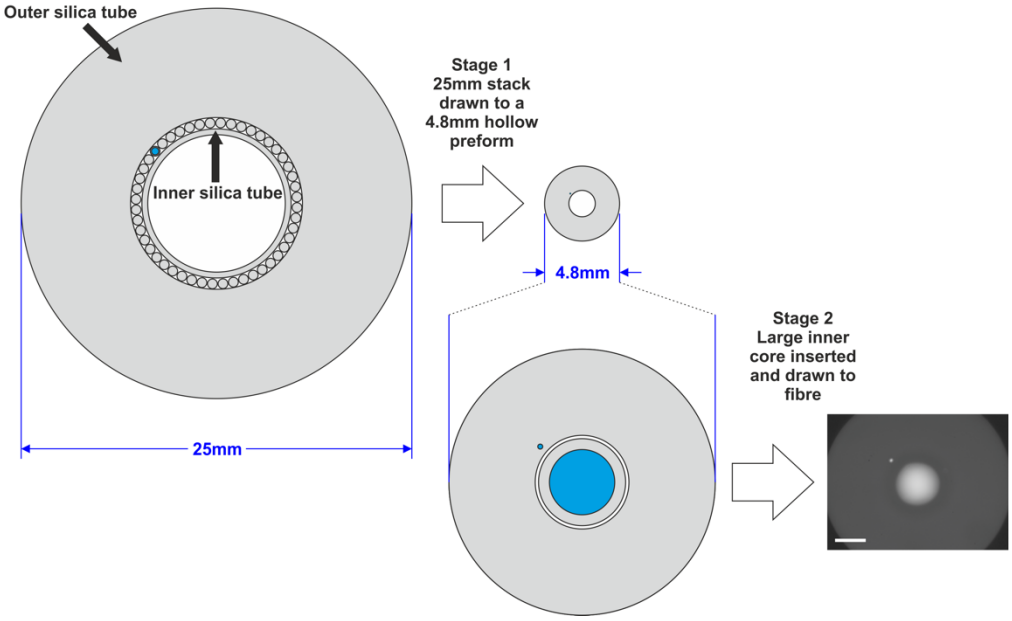

Fig. A1. Fabrication stages of the dual core fiber. Stage one, the formation of the stack to include the small excitation core. Pure silica rods (shown in grey) are stacked between two nested pure silica tubes, except that one of the rods contains a Ge-doped core (shown in blue) to form the small excitation core in the final fiber. Stage two, formation of the large collection core. A large rod with a Ge-doped core was inserted into the hollow preform drawn from the stack, then drawn down to form the final fiber. An optical micrograph of a transverse cross-section of the fiber is shown in the bottom right corner. The high-index core regions appear lighter in the image, with the small excitation core visible at "11 o'clock". The scale bar is 20 µm.

A.1 Fabrication of asymmetric dual-core fiber

The fiber was fabricated in two stages using a modification to the stack-and-draw method developed to make photonic crystal fibers [38]. Firstly, a stack to support the small SM excitation core was formed by placing undoped-silica rods, each 0.63 mm in diameter and 1.2 m long, in the circular gap between two nested silica tubes with outer/inner diameters of 25.0/11.0 mm and 9.5/8.8 mm respectively. The excitation core was included by replacing one of the rods with a rod drawn (on a fiber drawing tower) from a commercial MM fiber preform containing a Ge-doped graded-index core with a maximum numerical aperture of 0.3 (Fig. A1). This circular stack was drawn down to form a hollow preform. Secondly, the large multimode signal collection core was formed by inserting a rod drawn from the same commercial preform (but to a different size) into the void in the hollow preform. The whole assembly was then drawn down to form the final fiber. In both stages, unwanted interstitial air gaps were evacuated to collapse them during the draw and form a solid fiber. The small core had a slight elliptical deformation with a long axis less than 2 µm making the core single mode at the operating wavelength of 785 nm. The center-to-center core separation was 24 µm. The spacing between the cores and significant mismatch between core sizes meant that less than – 30 dB power was evanescently coupled from the excitation core to the signal collection core at the pump wavelength (785 nm) following propagation over a length of approximately 2 m when only the excitation core was excited at the opposite end.

A.2 Distal-end assembly

The distal end-cap for the optrode was fabricated by directly inscribing a three-dimensional support structure in a transparent (at 1030 nm) fused silica substrate (Corning) using focused (with a 0.4 NA aspheric lens) femtosecond pulses from a commercial micro-Joule fiber laser system (MenloSystems, BlueCut). The substrate was translated through the focus at a speed of 4 $mm.s^{-1}$ using high-precision air-bearing translation stages (Aerotech). Using suitable irradiation conditions (wavelength: 1030 nm, pulse duration: ~350 fs, repetition rate: 0.5 MHz, pulse energy: 550 nJ), the etching selectivity of the laser modified regions was enhanced [39] relative to the bulk material and subsequently dissolved in a dilute (5 %, aqueous) solution of hydrofluoric-acid within 2 hours. The end-cap, with a length of 1 mm and a maximum outer diameter of 1.2 mm, featured a 150 µm diameter inner slot to accommodate the 125 µm wide polymer-stripped section of the fiber optrode. The fiber-optrode and end-cap assembly was packaged inside a 2.5 m long protective biocompatible sheath (PEEK). Permanent bonding of the distal components was performed using ultraviolet curing optical adhesive (Norland NOA61).

A.3 SERS nanoshells preparation

Nanoshells (1 mL**,** $2x10^9$ particles/mL, ~ 150 nm, Bare AuroShell™ Particles in deionized water, Nanospectra Biosciences Inc.) were collected by centrifugation (5500 rpm, 10 min) and the supernatant was removed (800 µL). Distilled water (dH_2O - 900 µL) and p-MBA (100 µL, 1.0 mM in EtOH) were added to the remaining suspension. The nanoshell / p-MBA suspension was incubated overnight and excess p-MBA was removed by centrifugation (5500 rpm, 10 min). The supernatant was removed (1 mL) and the functionalized nanoshells were re-suspended in water (400 µL). The centrifugation wash step was repeated a further twice. After the final wash step, all but the final <100µL supernatant was removed and the functionalized nanoshells were re-suspended with sonication.

A.4 Poly-L-lysine preparation

Poly-L-lysine (0.1 mg/mL in distilled water, 30000-70000 MW, Sigma Aldrich).

A.5 Sol-gel preparation

The sol-gel was prepared as per Grant *et al.* [40], with the exception that MilliQ was used instead of deionized, distilled water.

A.6 pH buffer measurements

For on-bench calibration (see Section 3.1), p-MBA SERS spectra were acquired using the packaged miniaturized optrode from a total of 33 separate pH buffers within the pH 4.0 – 9.0 range. Of these, 21 pH buffers were prepared with pH increments of 0.1-pH units to sample the physiologically relevant pH 6.0 – 8.0 range. The pH 4.0 – 5.75 and pH 8.25 – 9.0 ranges were sampled using 8 and 4 pH buffers respectively, prepared in pH increments of 0.25-pH units. A SERS spectrum was obtained while the distal end of the optrode was submerged in each buffer for the duration of the spectral acquisition time. In total, 165 spectra were obtained, with the measurements split into 5 replicates, where a replicate consisted of placing the optrode in each of the 33 pH buffers. The order of the measurements within each replicate was random.

A.7 Ex-vivo ovine lung model

Ovine lungs were from ewes destined for cull and were euthanized under Schedule 1 of Animals (Scientific Procedures) Act 1986. Heart and lungs were excised from the culled donor sheep and immediately flushed with 0.9 % sterile NaCl (Baxter) (with the addition of Heparin sodium (LEO Laboratories Limited, Berkshire UK) at 500 $U.L^{-1}$ for perfusion models). Lungs were held on ice until commencement of ventilation, whereby they were placed inside a neonatal incubator (Druger Isolette C2000) and maintained at 35 °C, 50 % humidity. Lungs were prepared for ventilation using a soft tracheal tube (Rusch) and hand ventilation. Once recruitment was

observed for the whole lung, automated ventilation was initiated (Breas PV 403 PEEP) by gradually increasing respiratory rate to 12 breaths per minute and peak airway pressure approximately 30 cmH_2O. In order to bias lung tissue pH, 10 mL of each pH buffer (pH 2, 4, 6, 8, 10, 12) was instilled into anatomically distinct regions of the ovine lung through a Flexible APC Probe (ERBE USA Incorporated) inserted down the working channel of the bronchoscope (Pentax EPM-1000) to the distal lung. After 30 minutes of incubation (to allow buffer dispersal), the packaged fiber-optic optrode was inserted into the lung through the working channel of the bronchoscope to measure the tissue pH at each of the buffer instillation sites. Following the internal tissue measurements with the optrode, ventilation was ceased and each optical probe measurement site was measured by commercial tissue pH probe (Mettler Toledo) via small incisions made vertically through the lung. Measurements were taken from this central site and from ~5 mm either side of this in order to best sample the region the optical probe was inserted into. A comparison of tissue pH and blood pH was also measured in an EVLP model. To perform perfusion, a complete circuit was formed with the Peristaltic Pump (504 Du IP55 Washdown, Watson-Marlow) tube feeding into the pulmonary artery and out of the left ventricle to the collection reservoir. Any open blood vessels were clamped or sutured closed to prevent leakage of perfusate. The circuit was perfused with Hank's Buffered Salt Solution (HBSS, Gibco) supplemented with 5 % foetal bovine serum (FBS, Gibco) and 250 ml freshly harvested human blood. A total of 5000 U of heparin was added to the circuit in a final volume of 2 L. Ventilation was performed as previously described for 3 hours, with 500 µl blood samples removed from the circuit hourly. Ventilation was subsequently stopped, with continuing perfusion. Blood samples were then collected every 10 minutes for 60 minutes. All samples were probed with the commercial pH meter at the time of collection.